Core-shell iron oxide@stellate mesoporous silica for combined near-infrared photothermia and drug delivery : influence of pH and surface chemistry

Alexandre Adam[1], Sébastien Harlepp[2,3,4,5], Fiorela Ghilini[6], Geoffrey Cotin[1], Barbara Freis[1], Jacky Goetz[2,3,4,5], Sylvie Bégin[1], Mariana Tasso[6], Damien Mertz[1,*]

[1]Institut de Physique et Chimie des Matériaux de Strasbourg (IPCMS), UMR-7504 CNRS-Université de Strasbourg, 23 rue du Lœss, BP 34 67034, Strasbourg Cedex 2, France.
[2]INSERM UMR_S1109, Tumor Biomechanics, Strasbourg, F-67000, France.
[3]Université de Strasbourg, Strasbourg, F-67000, France.
[4]Fédération de Médecine Translationnelle de Strasbourg (FMTS), Strasbourg, F-67000, France.
[5]Equipe Labellisée Ligue Contre le Cancer.
[6]Instituto de Investigaciones Fisicoquímicas Teóricas y Aplicadas (INIFTA), Departamento de Química, Facultad de Ciencias Exactas, Universidad Nacional de La Plata - CONICET, Diagonal 113 y 64, 1900 La Plata, Argentina.
Corresponding author e-mail : damien.mertz@ipcms.unistra.fr

Abstract. The chemical design of smart nanocarriers, providing in one nanoformulation combined anticancer therapies, still remains a challenge in the field of nanomedicine. Among nanomaterials, iron oxide-based core-shell nanostructures have been already studied for their intrinsic magnetic hyperthermia features that may be coupled with drug delivery. However, despite the great interest today for photo-induced hyperthermia, very few studies investigated the potential of such nanocarriers to combine photothermia and drug delivery. In this work, our aim was to design functional iron oxide@stellate mesoporous silica nanoparticles (denoted IO@STMS NPs) loaded with a drug and able to combine in a same formulation near infrared (NIR) light induced photothermia with antitumor drug release. Herein, the NIR photothermal properties (SAR, specific absorption rates) of such nanomaterials were quantified for the first time as a function of the laser power and the NP amount. Aside the response to NIR light, the conditions to obtain very high drug loading (drug payloads up to 91 wt%) of the model antitumor drug doxorubicin (DOX) were optimized by varying different parameters, such as the NP surface chemistry (BARE (Si-OH), aminopropylsiloxane (APTES) and isobutyramide (IBAM)) and the pH of the drug impregnation aqueous solution. The drug release study of these core-shell systems in the presence or absence of NIR light demonstrated that the DOX release efficiency is mainly influenced by two parameters: surface chemistry (BARE ≥ IBAM ≥ APTES) and pH (pH 5.5 ≥ pH 6.5 ≥ pH 7.5). Furthermore, the temperature profiles under NIR light are found similar and independent from the pH range, the surface chemistry and the cycle number. Hence, the combination of local photothermia with lysosomal-like pH induced drug delivery (up to 40% release of the loaded drug) with these nanostructures could open the way towards new drug delivery nanoplatforms for nanomedecine applications.

Keywords: Iron oxide@mesoporous silica; Surface chemistry; Drug delivery; Near-infrared photo-induced hyperthermia

Graphical abstract
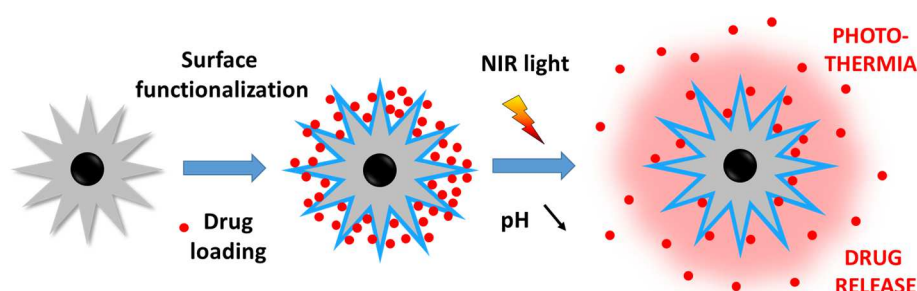
Introduction

Today, the use of smart or functional nanoparticles for the treatment of many diseases such as cancer has become a true medical challenge in the field of nanomedecine.[1,2] Such multifunctional nanoparticles, endowed with multiple imaging, targeting or therapy functionalities, are crucial for developing a personalized medicine, avoiding potential side effects and allowing enhanced therapeutic activity.[3–5] Among various existing reported nanosystems, iron oxide nanoparticles (IO NPs) are particularly appealing systems given their magnetic properties, low toxicity and biodegradability.[6,7] IO NPs have been mainly used in imaging and disease treatment given their magnetic properties. Indeed, they have been used as T_2 contrast agents for MRI,[8–10] they are known to have a limited toxicity and to be degraded within cells, being then less toxic to the organism as compared to other magnetic nanomaterials.[6,11–14] For instance, these external fields-responsive IO NPs show great promise as new theranostics for localized and remotely activated magnetic hyperthermia therapy[15–18] which may be followed with MRI. Upon alternating magnetic field application, they produce a local heat which is used for tumor treatment by magnetic field induced hyperthermia. This effect is already used in many preclinical studies and in the clinics,[19–21] with the example of MagForce in Berlin (Germany) where this effect is shown to promote cancer cell apoptosis.

Besides the magnetic field, another external field of interest is near infrared (NIR) light laser applications. Indeed, due to its simplicity and low cost, NIR light can be easily applied through a range of lasers with tunable power and wavelength. As compared to visible light, NIR light has a better tissue penetration in the 800 − 1300 nm range, reaching up to 3 cm.[22,23] NIR laser-induced hyperthermia is actually developed as a minimally invasive treatment where photothermal organic or inorganic sensitizers turn this absorbed light into localized heating at the nanoparticle scale.[24–28] For instance, the company Nanospectra Biosciences (USA) has clinically developed photothermal ablation based on gold@silica core shell nanoparticles for the treatment of prostate cancer and the non-toxicity of their gold and silica NPs was demonstrated.[29] As an alternative to gold nanoparticles, IO NPs have been recently shown to be attractive NIR light mediators and to have a great potential for photothermal treatment.[30–33] Recent studies demonstrate that NIR laser powers between 0.5 and 1 W.cm^{-2} combined with IO NPs are beneficial for in vitro phototherapy.

In addition to these hyperthermia treatments, the localized release of drugs remotely-stimulated by external fields is currently a great challenge. The design, in recent years, of organic, polymeric[34–37] or porous silica shells[38–40] around such iron oxide cores to control the magnetothermal response and to form a reservoir of drugs that can be delivered through these external fields to the target site paved the way towards very high achievements in the field of activated therapy and drug delivery.[41–45] Especially, with regards to the use of these NPs in a physiological medium, the NPs must be functionalized with appropriate surface ligands or shells to ensure colloidal stability, biocompatibility and drug loading and release. To address these latter problems, mesoporous silica (MS) as a shell coating is particularly attractive. Indeed, MS are stable, easily chemically modifiable and have a high drug loading/release capacity thanks to their large pore volume.[38,46–49] Moreover, given the possibility to render them stimuli responsive, especially for drug release, they are particularly suited for the treatment of various diseases[50–52]. In our team, we have

developed in-depth expertise in the synthesis of a range of MS nanostructures with well-controlled pore sizes (from 2.5 to 15 nm).[53–56] Recently we showed that the pore morphology of MS alone or as layers covering IO NPs can be easily oriented with the sol-gel reaction temperature either towards stellar (ST) (large radial pores of about 10 nm) for T ≤ 80 °C or "worm-like" (WL) morphologies (channels with random pores of 3–4 nm pore size) for T ≥ 80 °C.[56] The relaxometric (for MRI) and magnetothermal (SAR) characteristics of both core-shell NPs having respectively stellar or WL-type morphologies, were shown to be perfectly suited for MRI and magnetic hyperthermia applications. However, at this stage, their photoresponsive behavior, especially when they are loaded with drugs, has never been investigated.

Herein, we address for the first time the use of iron oxide core@stellate large pore mesoporous silica (denoted IO@STMS) for combined photothermal and drug release properties **(Figure 1)**. ST morphology has been chosen as their large pores promote the drug loading and improve heat dissipation from the central core to the surrounding medium. First, the photothermal properties of these core-shell NPs upon NIR light excitation were investigated by tracing temperature profiles and evaluating their specific absorption rates (SAR) in non-adiabatic conditions as a function of the laser power and the NPs' concentration. Secondly, the effect of key parameters, such as the pH of the drug impregnation aqueous solution, the surface chemistry or the presence of an iron oxide core (STMS vs. IO@STMS) on the drug loading capacity were unraveled. With the aim to cover the drug loaded core-shell NPs with a biocompatible layer, the adsorption of human serum albumin (HSA) onto this system was further studied in terms of NP-bound protein amount, and drug leaking after washings with buffers and after storage at 4 °C. The drug release of IO@STMS@DOX@HSA core-shell systems with a high drug loading (DLC ≥ 20%) was then evaluated as a function of the pH (pH = 5.5, 6.5, 7.5) and of the surface chemistry. A very classical way to improve drug loading/release on silica nanoparticles as compared to the BARE surface is the modification by aminosilane and particularly APTES[55,57,58] which is tested here with IO@STMS. In a more original way, the amine groups are then modified into isobutyramide (IBAM) functions which are known to favor immobilization of biomacromolecules like proteins.[59,60] The suitability of these three chemical functions to load and release DOX is studied. Cumulative drug release values were obtained after several daily cycles in the presence or absence of NIR light. Furthermore, the temperature profiles resulting from the application of the NIR light were plotted as a function of the pH, the surface chemistry or the cycle number to demonstrate the possibility of activating phototherapy at each cycle whatever the conditions.
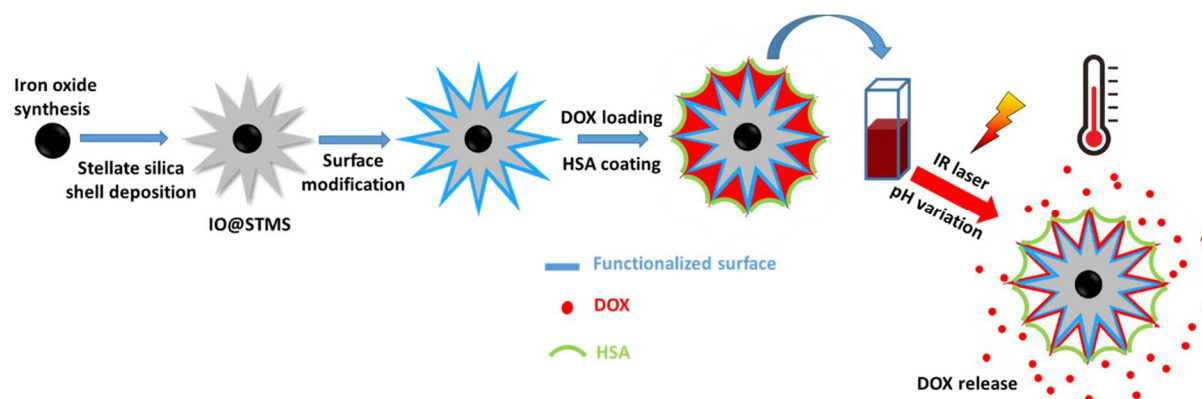
Figure 1. Schematic representation depicting the step-by-step preparation of drug loaded core-shell nanocomposites and the combined properties of NIR light-induced photothermia and pH-triggered drug release.

Materials & Methods

Chemicals. Tetraethyl orthosilicate (TEOS, ≥99.0%)), cetyltrimethylammonium tosylate (CTATos, ≥98.0%), 2-amino-2-(hydroxymethyl)-1,3-propanediol (AHMPD, ≥99.9%), ammonium nitrate (NH_4NO_3), (3-aminopropyl)triethoxysilane (APTES, 99%), isobutyryl chloride (IBC, 98%) and triethylamine (Et_3N, ≥99%) were obtained from Sigma–Aldrich (France). Nitric acid 70% (HNO_3, 70%) and N,N-Dimethylformamide (DMF, ≥99.9%) were purchased from Carlo-Erba. Ammonium hydroxide (25% in water) was obtained from Fluka. Iron(III) stearate ($FeSt_3$) was obtained from TCI. Oleic acid (99%) was purchased from Alfa Aesar while squalane (99%) was purchased from Acros Organic. Doxorubicin hydrochloride was obtained from OChem Inc. The Pierce BCA protein assay kit was from Thermo Scientific.

Iron oxide core synthesis. 1.9 g (2 mmol) of commercial $FeSt_3$, 1.9 g (6.7 mmol) oleic acid and 20 mL squalane were mixed in a two-neck round-bottom flask and heated to 110 °C for one hour to remove water traces and dissolve the components. Then the temperature was increased to 310 °C for two hours to start the thermal decomposition of the iron precursor. The iron oxide nanoparticles finally obtained were washed several times with hot acetone under stirring and collected thanks to a magnet. The washed iron oxide nanoparticles were then dispersed in chloroform for further use.

Synthesis of iron oxide core@stellate mesoporous silica (IO@STMS). To synthesize the mesoporous silica shell, the iron oxide cores need to be phase transferred into aqueous phase. Typically, 240 mg (0.53 mmol) CTATos, 27.6 mg (0.26 mmol) AHMPD and 25 mL distilled water were mixed in a 50 mL round-bottom flask. The mixture was heated up to 50 °C for 30 min to dissolve every chemical. Then, 10 mg of iron oxide nanoparticles dispersed in chloroform were added under strong agitation and the temperature was increased to 65 °C in order to evaporate the chloroform. The mixture was let to stir at 65 °C for 30 min. Afterwards, 2 mL of TEOS were added, the temperature was increased to 70 °C and the reaction was let to stir for two hours. The reaction was stopped by cooling down the mixture and followed by centrifugation at 12,000 g for 12 min to recover the nanoparticles. The particles were washed twice with 15 mL of a mixture of distilled water and ethanol (1:1). The templating surfactant was removed by dispersing the nanoparticles in NH_4NO_3 ethanolic solution (20 mL, 20 mg.mL^{-1} in EtOH) under stirring and heating at 70 °C for one night (16 hours). Then the nanoparticles were washed once with 20 mL distilled water and twice with 20 mL absolute ethanol. The extraction efficiency was checked by zeta potential (ZP) analysis. Before extraction, the ZP is positively charged as the CTA$^+$ surfactant, adsorbed on the IO@STMS, governs the NP charge. During the CTA$^+$ surfactant extraction, the NP reverses its surface charge and the extraction is considered completed when the ZP has reached a plateau of negative ZP values (usually −20 to -30 mV in water at pH = 7.5, bare silica). The extraction with ammonium nitrate solution had to be repeated several times. Finally, the synthesized core-shell IO@MS were dispersed in ethanol and kept in the fridge at 4 °C for storage.

Dosage of iron in the core shell NPs. The concentration of nanoparticles was determined by drying a fixed volume of the dispersion (typically 100 µL) and weighting the powder. Then, to calculate the amount of iron, the dried powder was digested with nitric acid 65 wt% in order to dissolve the iron oxide core. The sample was then diluted to get a 2 wt% HNO_3 solution.

The T_1 relaxation time of the solution was measured and, thanks to a pre-established calibration curve, the amount of iron was determined.

Synthesis of stellate mesoporous silica (STMS). To obtain stellate mesoporous silica NPs, 3.8 g (8.3 mmol) CTATos and 0.436 g (4.15 mmol) AHMPD were dissolved in a 500 mL Erlenmeyer flask with 200 mL distilled water. The mixture was heated up to 65 °C to ensure full dissolution. Afterwards 30.2 g (32.1 mL, 145 mmol) TEOS were added under agitation. 15 min later the temperature was set to 70 °C. Two hours after TEOS addition, the reaction was stopped by cooling down the mixture to room temperature. The NPs were collected by centrifugation (13,000 g; 15 min) and calcinated in an oven at 550 °C for 6 h. Finally, the STMS NPs were crushed with a mortar and dispersed in ethanol for further use. The concentration of STMS was determined by drying a precise volume of the dispersion and weighting the powder.

APTES functionalization (IO@STMS@APTES). 10 mg of core-shell IO@STMS were dispersed in a centrifuge tube in 2.75 mL of absolute ethanol. Then 150 µL of aqueous ammonia $NH_{3(aq)}$ 25% and 625 µL of APTES were added successively. The reaction was performed at room temperature for two hours and continuously stirred on a stirring wheel at 40 rpm. The nanoparticles were then centrifuged (12,000 g, 10 min) and washed twice with 5 mL ethanol.

IBAM functionalization (IO@STMS@IBAM). The previously synthesized IO@STMS@APTES were washed twice with DMF and centrifuged (12,000 g, 10 min). The supernatant was removed and 1.5 mL of DMF and 200 µL of Et_3N were added. The mixture was vortexed and sonicated to disperse properly the nanoparticles. Afterwards a mixture of 275 µL of IBC dissolved in 1.5 mL DMF was added to the particles' dispersion. The reaction was let to stir on a mechanical wheel for two hours. Then, 1 mL of distilled water was added to dissolve the ammonium chloride precipitate formed during the reaction. Finally, the nanoparticles were recovered by centrifugation (12,000 g, 10 min) and washed twice with DMF.

Loading of doxorubicin (DOX). Typically, 2.5 mg of core-shell nanoparticles, functionalized or not, i.e. IO@STMS, IO@STMS@APTES or IO@STMS@IBAM, were washed twice with an aqueous 100 mM HEPES buffer at a defined pH (5.5, 6.5 or 7.5). Then 1 mL of DOX solution at a given concentration in the same buffer was added and agitated for 24 h on a mechanical wheel at room temperature and in the dark. After loading, the supernatant was removed by centrifugation (14,000 g, 10 min) and the nanoparticles were washed twice with HEPES buffer. Every supernatant was collected and stored for analysis. The amount of DOX in the supernatant was determined by UV-Vis spectrophotometry at 480 nm. The total DOX amount on the three supernatants was determined and subtracted to the DOX amount used during loading to obtain the DOX loaded amount per mg of NP.

Immobilization of human serum albumin (HSA). After doxorubicin impregnation, the nanoparticles were coated with HSA. For this, 2.5 mg of drug-loaded nanocomposites were dispersed in 0.625 mL of an HSA solution in 100 mM HEPES pH 7.5 at 400 µg mL^{-1}. The dispersion was stirred on a mechanical wheel for 1 h at room temperature and in the dark, then centrifuged (12,000 g, 12 min) and washed twice (12,000 g, 12 min) with 2 mL HEPES buffer pH 7.5.

Quantification of HSA. The three supernatants resulting after centrifugation and washings were kept and used to quantify the unbound HSA amount by means of the bicinchoninic acid (BCA) test. The principle of this assay relies on the reduction of copper ion Cu(II) into Cu(I) by the peptide bonds in proteins. Then, BCA forms a purple complex with Cu(I) specifically. The absorbance of the solution depends on the amount of reduced Cu(II) which is proportional to the amount of proteins in solution. As for the drug, the obtained amount was then subtracted to the amount employed during HSA incubation to obtain the protein amount bound to the NP. In the BCA reaction, the supernatant (100 µL) was mixed with the BCA reagent (20 µL) in a 96 well plate and left at 45 °C during 1 h. Afterwards, the absorbance at 562 nm was read. The obtained absorbance is compared with a calibration curve to obtain the HSA concentration per well.

NIR laser irradiation and DOX release. 1 mL of DOX-loaded nanocomposite suspension at 3 mg.mL^{-1} in 100 mM HEPES buffer at different pHs was added into a 1 mL plastic cuvette placed in a dedicated sample holder in front of the laser output. The laser was then switched on and the sample was irradiated for 45 min; then the laser was switched off. The power of the laser was fixed at 1 W.cm^{-2} and the temperature elevation of the suspension is recorded by a thermocouple. Afterwards, the sample was centrifuged (10,000 g, 10 min) in order to collect the supernatant. The concentration of released DOX was determined by UV-Vis spectrophotometry as explained above. Fresh HEPES buffer was then added, the particles were redispersed by sonication and agitation, and a new irradiation cycle of 45 min was performed. In total, each sample were irradiated four times. The effect of the pH on the release was studied by adjusting the pH at 5.5, 6.5 or 7.5.

Characterization techniques

Fourier-transform infrared spectroscopy (FTIR). FTIR spectra were recorded for wavenumbers between 4000 and 400 cm^{-1} on a Spectrum 100 from Perkin Elmer. Few drops of the dispersions were added to dry KBr. After grinding and pellet formation, FTIR transmittance spectra were measured.

Transmission electron microscopy (TEM). The IO@STMS and STMS NPs were deposited on carbon-coated copper grids. TEM images were acquired with a JEOL 2100 TEM instrument operating at 200 kV. The software Image J was used to determine the size distribution of the NPs.

X-ray diffraction analysis (XRD). X-ray diffraction (XRD) patterns were recorded at room temperature with a Brucker D8 Discover diffractometer equipped with a Lynx-Eye detector in the 20-70° (2θ) range with a scan step of 0.03° and the sample rotates at 30 rpm during the measure. Silicon powder was used as internal standard. The diffraction peaks were compared to JCPDS database.

Thermogravimetric analysis (TGA). The thermogravimetric analysis (TGA) was performed on a STD Q600 (TA Instruments). The runs were started from room temperature to 800 °C with a heating rate of 5 °C/min, under an air flow rate of 25 mL/min.

Dynamic light scattering (DLS). Hydrodynamic size distributions and colloidal stability of the nanoparticles at different stages (i.e. with and without HSA, with and without DOX, and after storage at 4 °C during several days or weeks) were obtained in a Malvern Nanosizer instrument operating at room temperature. Prior measurements, samples were sonicated during 15 min and redispersed in a suitable buffer. Samples were measured in Milli-Q water (pH 5), 10 mM PBS (phosphate buffer saline), pH 7.4 and in 100 mM HEPES buffer, pH 7.5. Intensity and number distributions were obtained.

RESULTS AND DISCUSSIONS

1.   Photothermal properties of iron oxide@stellate mesoporous silica nanoparticles

First, IO NPs playing the role of NIR light sensitive core materials were synthesized by the thermal decomposition method according to previously reported works.[61,62] TEM images indicated the formation of homogenous spherical iron oxide NPs with a mean diameter of 28 nm diameter (**Figure 2**). The X-ray diffractogram confirmed the presence of only the spinel phase structure while FTIR spectra confirmed the successful washing with the presence of only Fe-O IR bonds as well as those of the fatty acid (carboxylate and alkyl chain bands) (See **Figure S1-S3** for TEM, XRD and FTIR of the IO NPs). Magnetic properties of such iron oxide cores, such as their superparamagnetic behavior and suitable saturation magnetization values have been described in detail in previous works [63,64]. Then, a stellate mesoporous silica (STMS) shell with controlled thickness and porosities was deposited around the iron oxide cores. CTATos was used as a porogenic surfactant yielding to stellate large pores after the sol gel reaction, as previously reported.[56,65] The surfactant was removed by extraction with ammonium nitrate in an ethanolic solution. TEM images showed the formation of individual and homogenous core shell NPs with large pore size (ca. 100 nm) (**Figure 2.A**) while DLS showed excellent colloidal dispersion in ethanol or aqueous buffer (**Figure S4**) as previously described.[53] Pore sizes of such STMS NPs were shown to be usually in the range of ca. 10-15 nm and specific areas in the range of 500-700 $m^2.g^{-1}$.[53,56]
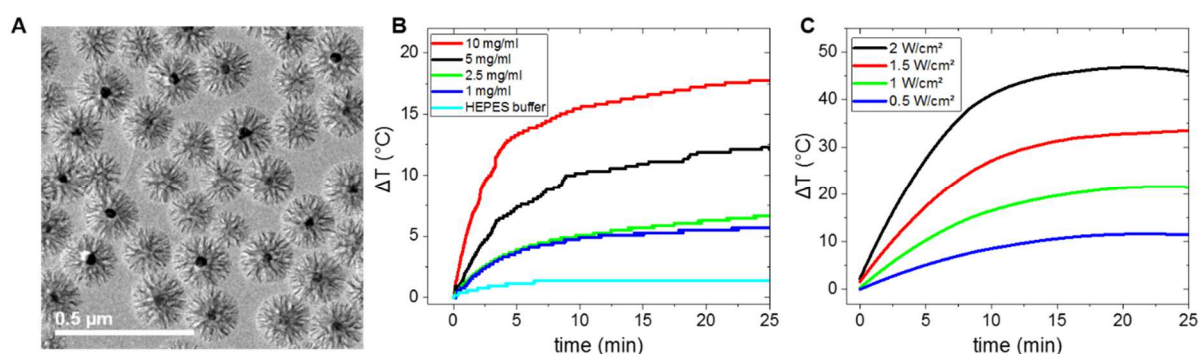
Figure 2. TEM image of the synthesized NPs (A) and temperature elevations under NIR laser at 1 W.cm^{-2} for different NPs concentrations (B) and for different laser power, at a NPs concentration of 5 mg.mL^{-1} (C).

The photothermal properties of these core-shell NPs were evaluated by measuring the temperature elevation of aqueous dispersions when exposed to NIR light (1064 nm). This wavelength presents a good optical transparence in water and in biological tissues. Moreover,

the YAG crystals, emitting at 1064 nm, are easy to process and allow to obtain high laser power which make them frequently used in research but also in industry for their very competitive power to cost ratio. At this wavelength, it is reported that spinel phase iron oxide can absorb the radiation and, by a non-radiative decay, converts it into dissipated heat.[66] The influence of NPs concentration (**Figure 2.B**) and laser power (**Figure 2.C**) on temperature profiles was investigated. First, the data indicate that suspensions heat up quickly under irradiation by NIR light. Temperature elevations between 5 and 40 °C can be easily obtained as a function of the experimental conditions. This also indicates that it is possible to finely tune and control the amount of dissipated heat which is fundamental for medical applications where a precise temperature range has to be attained. In this non-adiabatic experimental set-up, temperature plateaus were reached rapidly after 5 to 10 min irradiation.

As an analogy to the magnetothermal transfer, the photothermal transfer can be calculated as the specific absorption rate (SAR) in watt per gram of iron oxide absorbing NIR light. This value was calculated by a calorimetric method. By plotting the temperature profiles of the NPs' suspensions subjected to NIR light and then adjusting the experimental curve with a polynomial function the $[dT/dt]_{t=0,s}$ can be determined. Water and aqueous buffer solutions are almost transparent to the excitation light at 1064 nm and absorb very little the radiation. In order to perform precise calculations, the contribution of the solvent in the temperature elevation has to be removed. The calculation of the SAR is thus summed up as:

$$\text{SAR} = C_s \cdot \frac{m_s}{m_{Fe}} \cdot \left(\left[\frac{dT}{dt}\right]_{t=0,s} - \left[\frac{dT}{dt}\right]_{t=0,buffer} \right)$$

where m_s and C_s are respectively the mass (g) and the heat capacity (J.g^{-1}.K^{-1}) of the sample, m_{Fe} (g) is the mass of iron oxide present in the sample, $(dT/dt)_{t=0,s}$ the derivative function of the temperature at $t = 0$ (K.s^{-1}) for the measured sample and $(dT/dt)_{t=0,buffer}$ the derivative of the reference buffer.

It is worthy to note that when the NP concentration increases from 1 to 20 mg.mL^{-1} (from 0.013 to 0.26 mg[Fe$_3$O$_4$].mL^{-1} respectively), the SAR values (measured at a fixed power of 1 W.cm^{-2}) decrease from 2014 to 453 W.g^{-1} (**Figure 3.A**). An explanation is that at high concentrations, the penetration depth of the laser in the sample is limited due to light absorption by dispersion.[67,68] Thus the incident light cannot be equally distributed in the whole sample, as the NPs in the front of the cuvette would absorb and scatter most of the light. This leads to a gradient of incident power in the sample and in average the NPs absorb less.[69] Furthermore, we investigated the effect of the laser power (at a fixed concentration 5 mg.mL^{-1}) and an exponent-like growing evolution of SAR was obtained. This non-linear effect could be attributed to a better penetration of the laser beam into the sample (**Figure 3.B**).

Overall, it can be concluded that the NPs' concentration and the laser power influence considerably the photothermal SARs. In very recent reports, the effects of silica clustering or encapsulation around IO NPs, on the photothermal heating were investigated.[69,70] Photothermal SAR values (with laser power set at 0.3 W.cm^{-2}, at 808 nm) were shown to decrease from ca. 2000 to 200 W.g^{-1} when increasing NPs concentrations (iron concentration range of 10-150 mM), which is overall in agreement with our SAR results. These values obtained are also comparable to previously published magnetic SARs in usual conditions of frequency and fields (H = 500 G, f = 536 kHz). The SAR values obtained here with the

photothermal approach are found of the same order of magnitude than the magnetothermal approach,[67] *i.e.* in the range of 1000-2000 $W.g^{-1}$ with laser power compatible with biomedical applications ($\leq 1W.cm^{-2}$). For higher laser power ($\geq 1\ W.cm^{-2}$) these SAR values can even be multiplied several times. This demonstrates the high feasibility of the iron oxide core@mesoporous silicas for photothermal therapy applications.
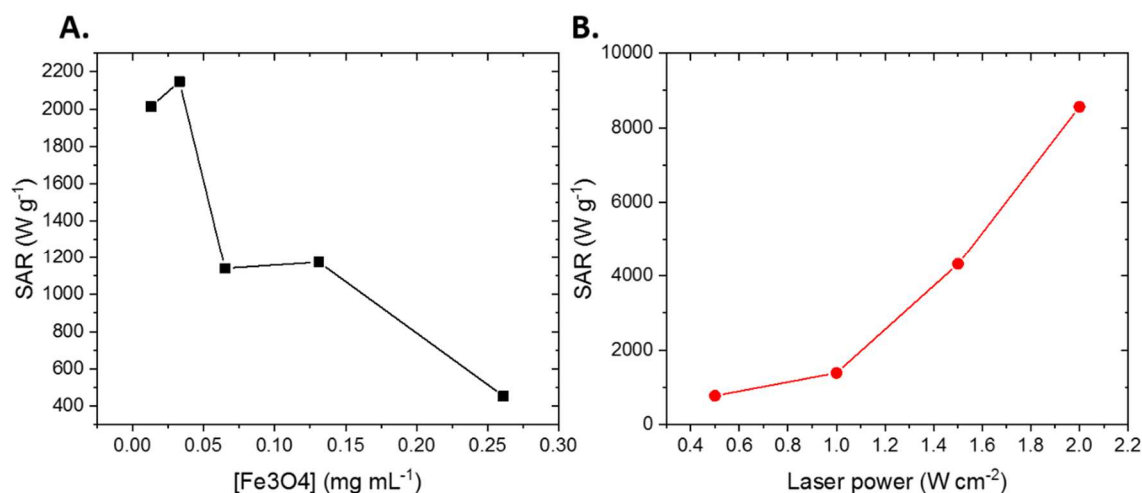
Figure 3. SAR values evolution (A) for different concentrations of core shell NPs and corresponding iron oxide amount and (B) for different laser powers at 5 mg mL^{-1}.

2. Drug loading study as a function of the pH and the surface chemistry

In this study, our aim was to produce a nanoplatform having two different antitumor effects: photothermal therapy and drug release. By modifying the surface chemistry of the IO@STMS core shell NPs, our aim was to engineer a suitable surface to i) load efficiently the IO@STMS NPs with a very high amount of the antitumor drug, doxorubicin (DOX) and also ii) to ensure a suitable wrapping of the NPs with a tight serum albumin coating around the NPs to provide gate keeping (drug retention), and to afford a strategy limiting immune system clearance. This would ensure the production of a nano-object able to perform tissue imaging (T2 weighted-MRI due to the iron oxide core) as well as treatments by phototherapy and chemotherapy (drug delivery).

In previous works, we developed structurally equivalent functionalized mesoporous stellate silica nanoparticles without any iron oxide core.[59,71] In this section, the grafting of functional groups is compared between the stellate silica NPs with iron oxide core (IO@STMS) and without (STMS). The NPs without IO core were chosen to assess the relevance of the surface functional groups into the DOX loading capacity. They represent an alternative to the core-shell nanostructures for the assessment of these phenomena as they can be synthesized at a very large scale reproducing the same pore structures. These STMS NPs had similar size as the IO@STMS (**Figure S5**) but lack the IO core.

To study the effect of the functionalization on the drug loading capacity of the NPs, the first step was to modify the BARE's surface with an aminosilane, 3-aminopropyltriethoxysilane (APTES). The reaction was performed in ethanol and catalyzed by the addition of ammonia. This leads to the APTES NPs. Then a further functionalization was carried out by reaction with isobutyrylchloride to get isobutyramide functional groups. These particles were denoted as

IBAM NPs. **Figure 4.A** summarizes these reaction steps. A DLS size analysis was realized on the three STMS surfaces: BARE, APTES and IBAM. The colloidal stability was studied in water and in HEPES buffer 100 mM. BARE STMS NPs were shown to disperse very well in water and in HEPES. STMS@APTES and IBAM tend to agglomerate in HEPES while their behaviors in water are better improved (**Figure S6**). Nevertheless, these results ensure suitable DOX loading and HSA coating studies in the next sections.
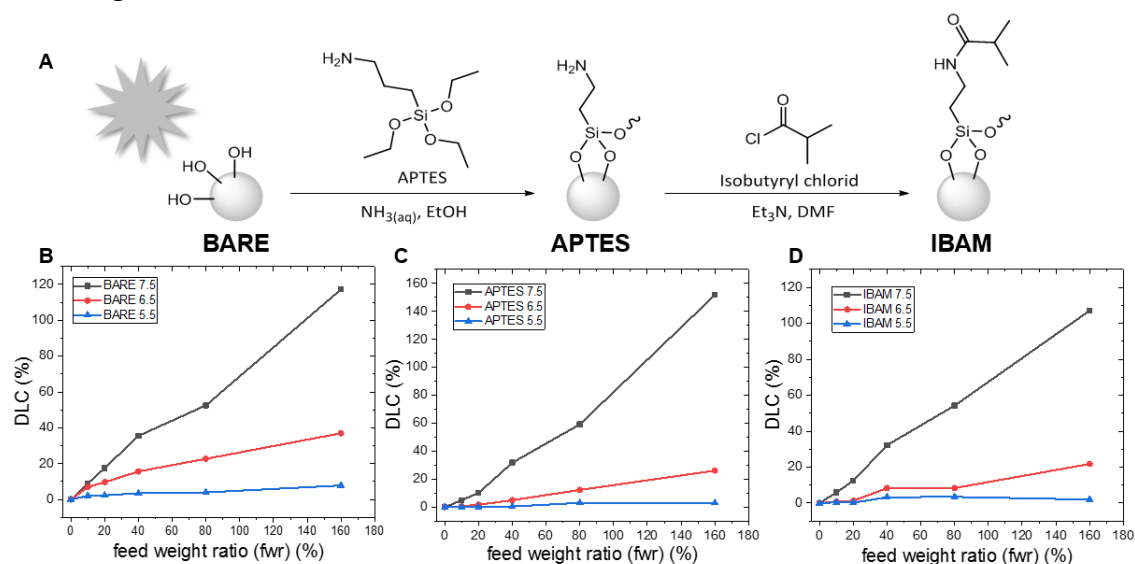
Figure 4. Chemical route to obtain the different surface chemistries (A) and the corresponding DLC of BARE (B), APTES (C) and IBAM (D) surfaces at the three evaluated pHs.

Once modified, we investigated the drug loading capacity (DLC) of each type of particle. The DLC is defined as the amount of DOX loaded onto and into the nanoparticle divided by the mass of NPs. Moreover, DOX is known to be sensitive to pH, in physiological aqueous solutions, especially due to the protonation of the osamine into ammonium groups (pKa1= 8.2) (**Figure S7.A** for DOX chemical structure). DOX source itself is quite acidic as the soluble form of DOX used is doxorubicin hydrochloride. Thus, to ensure a good control of the loading conditions, HEPES buffer at 100 mM was used as loading dispersion medium and adjusted with HCl or NaOH to precisely set three different pH at 5.5; 6.5 or 7.5. These three pHs are known to be of biological relevance (endolysosomal vesicles, extratumoral tissues, in vivo blood, respectively). Here, the DLC is defined as the amount of loaded DOX, while the feed weight ratio (fwr) is used to characterize the amount of DOX given during the loading.

$$DLC = \frac{\text{mass of loaded DOX put in NPs}}{\text{mass of NPs}}$$

$$fwr = \frac{\text{mass of DOX put in solution}}{\text{mass of NPs}}$$

DOX payloads were thus evaluated by spectrophotometry analysis of the supernatant and using calibration curves (**Figure S7.B** for DOX calibration curves at the three pHs). The results show that for all three surfaces, the pH of the DOX solution is a determinant factor of loading (**Figure 4.B-D.** for pH = 5.5; 6.5; 7.5). While for pH = 5.5, DOX shows almost no loading even at high feed weight ratios (for example on IBAM NPs, DLC = 2.0% at fwr = 160%), the DOX

loading at pH = 6.5 showed slight increase of DLC (DLC = 21.8% at fwr = 160% for the same IBAM NPs) and the DOX loading considerably exploded at pH = 7.5 for the different fwr used (for example on IBAM NPs DLC = 107.1% at fwr = 160%). Thus, very high amounts of drug can be loaded on these NPs by selecting the most convenient loading buffer. By increasing the pH at 7.5 and using appropriate DOX concentrations, it is possible for these NPs to carry more than 100% of their own mass. Such high DLCs were previously obtained in our team on CNTs@MS@APTES[55] and CNTs@MS@IBAM[72] and here they are demonstrated for the first time on IO@STMS NPs. Worthy to note that such high DLCs are few reported in the literature on iron oxide@MS-based nanomaterials where usual DLCs are in the range 10-40%.[73,74]

To explain this result, the behavior of DOX is influenced by several parameters, as the pH and the ionic strength of the medium. DOX contains two mild acid/base couples in its structure, one on the amine function of the osamine group with a pKa at 8.2 and the other one is carried by the hydroxyl group on the C11 with a pKa at 9.5. In the pH range used (5.5-7.5), it has technically one acidic proton (NH_3^+/NH_2) group which is crucial to DOX solubility. Furthermore, in this pH range, it has been shown that DOX can auto-assemble into dimers like all anthracycline molecules but also into bigger structures, aggregates or gel which is more peculiar.[75–77] These self-assembly phenomena can be explained by the fact that when increasing the pH from 5.5 to 7.5, the proportion of the neutral amine form grows, and electrostatic repulsions are decreased, limiting the fraction of individual molecules. A pH increase from 5.5 to 7.5 will thus increase the DOX self-aggregate sizes. This neutral form tends to build supramolecular polymer-like aggregates made of hundreds of units.[78] Weak interactions like dipolar interactions, but especially stacking of π systems and numerous H-bonds, may lead to these associations. It is thus assumed here that the very particular structure of DOX is responsible for such assembly behavior and may explain the achievement of such high DLCs .[77]

Once the behavior of the STMS NPs could be determined regarding their DOX loading capacity at different pHs and for various surface ligands, the same was carried out onto the core-shell IO@STMS. DOX was loaded in 100 mM HEPES buffer at pH = 7.5, the DLCs were calculated and compared to those obtained for NPs without an iron oxide core (**Figure 5**). On the BARE NPs, DLCs are relatively similar for STMS and IO@STMS from low to high fwr. However, a clear difference can be observed for the APTES and IBAM NPs: DLC on IO@STMS were half the ones obtained for STMS, especially for APTES and IBAM-functionalized NPs. To explain these differences, TGA was performed on STMS and IO@STMS and results indicate a better grafting of APTES on IO@STMS (18.9% wt) vs. STMS (13.3% wt), respectively (**Figure S8**). STMS NPs are calcinated at 550 °C after synthesis to remove the surfactant whereas for IO@STMS the surfactant is chemically removed to preserve iron oxide core from phase transformation. This calcination may lead to more silica condensation of the STMS, which means less active hydroxyl groups at the surface (hydroxyl groups condense to form bridging oxygen bonds between two silicon). As a consequence, less APTES reacts with the STMS surface, which allows more pore volume for DOX diffusion and ensures that more DOX can be loaded in the STMS NPs. Additionally, as compared to the core free STMS NPs, the large pore STMS silica shell formation onto IO cores may result in a loss of the interconnectivity of the pores, which reduces also the pore volume available for drug loading for these IO@STMS NPs.
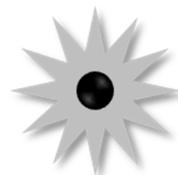
fwr %	BARE %	APTES %	IBAM %
20	17.6	10.1	12.4
80	52.5	59.2	54.2
160	117.3	151.7	107.1

fwr %	BARE %	APTES %	IBAM %
20	18.3	5.95	6.94
80	55.2	23.9	25.0
160	91.1	64.0	73.4

Figure 5. DLCs obtained for the three surfaces at pH 7.5 for STMS (left) and IO@STMS (right) NPs at various fwr.

3. Study of drug leaking effects and human serum albumin adsorption

Another crucial aspect for the design of this nanoformulation, is to ensure a limited leaking of the loaded DOX from the NPs, in order to handle and store the NPs before use. DOX loaded IO@STMS (BARE, APTES and IBAM-functionalized) NPs at the DLC in the range 20-45% as analyzed before, were consecutively washed with fresh loading buffer (HEPES 100 mM, pH = 7.5) and their supernatants were analyzed by UV-Vis spectrophotometry to determine the amount of DOX leaked during this washing process (**Figure S9.A**). Here, DOX loading was carried out at pH 7.5, as for the releasing buffer. The leaking was evaluated by repeated washings of the DOX-loaded NPs by centrifugation cycles. After one washing step (W1 in the figure), less than 10 % of the initially loaded DOX was leaked in all types of surfaces. Subsequent washings (W2 – W4 in the figure) induced a leaking ranging from 1 to 6 %. The spontaneous loss of DOX (at room temperature and at pH 7.5) is thus moderate in the first washing step and then very limited. It is also noticeable that for higher fwr, i.e. high DLCs, the proportion of DOX that spontaneously leaks out is reduced. By promoting the supramolecular assembly of DOX, the pores are filled with the drug and both the surface area as well as the accessibility of the solvating aqueous solution to the DOX molecules may be reduced which may explain why less drug is leaking.

The stability upon storage was also checked by leaving the same DOX loaded samples at 4 °C for one week. Here, the pH of the storage buffer was also adjusted and the fwr was fixed at 80%. After centrifugation, the amount of DOX leaked during this period was evaluated as compared to the initially loaded DOX. **Figure S9.B** clearly shows that by increasing the acidity of the storage liquid medium, more DOX was released from the NPs for each and all types of surface functionalization. The other interesting aspect is that BARE NPs were the most leaking formulation whereas APTES was the least one (ca. 25 vs. 5% at pH 7.5 over 1 week, respectively). IBAM leaks intermediately between these two.

Having evaluated the DOX release behavior after consecutive washings and upon storage at 4 °C during one week and in different pHs, it became clear that the nanosuspension slowly but steadily releases a rather small proportion of the DOX loaded to the medium. For further biological applications, this spontaneous DOX leaking has to be minimized. The

addition of an external biocompatible coating would avoid this leaking and prevent the direct contact between the drug-loaded NP and the biological tissues. Human Serum Albumin (HSA) protein has been chosen in order to improve the biocompatibility of the NPs as well as to reduce opsonization of the nanoformulation. Before the HSA adsorption step, DLCs of DOX were previously calculated after DOX impregnation and two consecutive washings (see **Table S1**, DLC before and after two washing steps). Then, at physiological pH, negatively charged HSA was adsorbed onto positively charged DOX-loaded NPs for the three surfaces (BARE, APTES and IBAM). The amount of coated HSA on the NPs was determined by spectrophotometry using bicinchoninic acid (BCA) assay (see details in Materials and Methods section). The calibration curve is shown in **Figure S10**. A feed weight ratio of 100 µg of HSA per mg of IO@STMS NPs was introduced during the HSA adsorption step. Analysis of the HSA amounts in the supernatants (after two washing steps) by the BCA assay (**Figure S11)** allowed to determine coatings in the range 51-81 µg(HSA).mg(NP)$^{-1}$. These results showed a quite effective HSA coverage (**Table 1**, top line) for the three surfaces used. Furthermore, the amount of DOX released during the protein coating and after two washings was measured for each surface (**Table 1**, bottom line). The lost quantities at this step were very low even if it can be noted that the BARE surface is the one that released the most. The final DLCs of the NPs correspond at this stage to the DLCs after HSA immobilization, taking into account the DOX leaked following washing steps.

**Table 1.** Amount of coated HSA and DOX released during the protein coating reaction.

	BARE	APTES	IBAM
HSA coating(µg/mg IO@STMS)	51.2	81.6	62.2
DOX leaking during HSA coating (% of DLC)	5.3	0.6	3.1

Overall, these characterizations have shown that the formulations described here are good candidates to combine photothermal therapy and drug delivery as it is possible to load them with high amounts of DOX as well as to induce significant heating upon NIR irradiation.

4.   Drug release study as a function of pH, surface chemistry and NIR light applied

In a next step, we thus studied the drug release behavior of core-shell NPs loaded with DOX (obtained for equal DOX fwr), coated with HSA, and having intermediate DLCs (BARE : 45%, APTES : 18% and IBAM : 27%, all loaded in HEPES 100 mM, at pH 7.5). NIR light irradiation was also applied to the different surface-functionalized IO@STMS NPs (BARE, APTES, IBAM). As the pH played a major role in the DOX loading and leaking studies, we also investigated this parameter on the release, by using HEPES buffer 100 mM at three different values (pH= 5.5, 6.5, 7.5). 1 mL of DOX-loaded NPs were introduced into a plastic cuvette. Then, the laser was switched on and the sample was irradiated at 1064 nm from one side of the cuvette with a power of 1 W.cm^{-2} **(Figure 6.A**). After 45 min, the laser was switched off and the supernatants were collected by centrifugation. Fresh buffer was added to the NPs and irradiation was repeated. In total four cycles were achieved on each sample.

For each functionalization (BARE, APTES and IBAM), and each pH, the amount of DOX released during the irradiation was measured and compared to the control sample which was not irradiated (**Figure 6.B-D, left)**. Associated heating curves showed that the temperature elevation profiles remained similar in every tested condition (**Figure 6.B-D, right**). Indeed, the pH, the functionalization state of the silica shell and the repeated heating cycles did not degrade the heating performance of the iron oxide core. At higher pHs, some cooling can be seen after ten minutes laser irradiation. This may be due in some cases to sedimentation of the NPs at the bottom of the cuvette. pH 5.5 better stabilized the dispersion because in the core-shell NPs (IO@STMS@DOX@HSA), the DOX charge governs the NP surface charge, which is positively charged at pH 5.5. For instance, by decreasing the pH from 7.5 to 5.5, zeta potential values increased respectively for IO@STMS@DOX@HSA (BARE from −7.8 to +14.4 mv) and IO@STMS@IBAM@DOX@HSA (IBAM from −5.6 to +33.6 mV) NPs. This ensures better electrostatic repulsions between the NPs and thus a better colloidal stability.
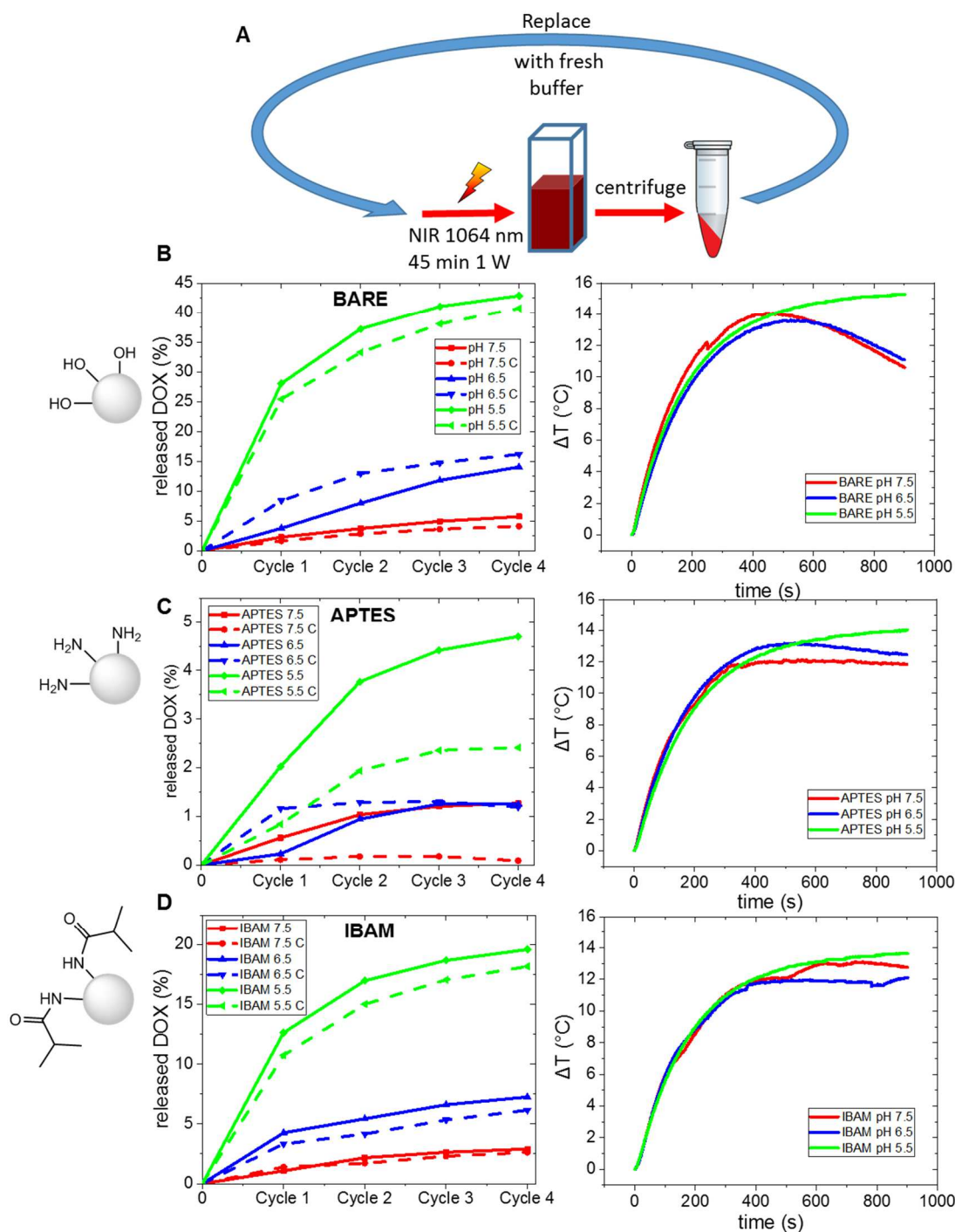
Figure 6. (A) Scheme of the NIR light irradiation protocol. Graphs on the left are the cumulative amounts of released DOX for the BARE(B), APTES(C) and IBAM(D) surfaces. Bold lines correspond to NPs with NIR light and dotted lines without NIR light applied. Graphs on the right correspond to temperature elevation curves of the NP suspension upon NIR light. C means no NIR light applied.

Observations from Figures **6.B-D** indicate that the temperature elevation induced by the NIR laser influenced very little the DOX delivery. Regarding the cumulative drug release curves, usually about half of the total DOX was delivered during the first cycle and the delivery was more sustained throughout the following irradiation cycles. Furthermore, for each surface state, the main parameter to control the release was the pH of the buffered dispersion. At pH

7.5, a very limited amount of the total loaded DOX was released for all three surfaces. These amounts were more than doubled at pH 6.5, and importantly increased at pH 5.5, which are suitable acidic pHs respectively for drug release in tumor tissues and in lysosomes. For example, in the case of BARE NPs, along the cumulative release, DOX release was of ca. 5.7, 14.0 and 42.8% when decreasing respectively the pH at 7.5, 6.5 and 5.5.

However, even if this trend (increasing DOX release by decreasing pH) was also found for the APTES and IBAM surfaces, it is worthy to remark the important influence of the surface chemistry on the % amount of drug released. **Figure 7** represents the evolution of the total % drug released (from the cumulative release study of **Figure 6**) as a function of the surface chemistry and the pH. This graph shows clearly that whatever the pH, the amount of DOX released from the chemically modified IO@STMS NPs follows this order : BARE ≥ IBAM≥ APTES. For instance, at pH = 5.5, DOX release from the three different surfaces was found to be ca. 40% for BARE, 17% for IBAM and only 2% for APTES (for no NIR light applied). The different DLCs (BARE : 45%, APTES : 18% and IBAM : 27%) do not explain this behavior as in the leaking study (**Fig S9.A**), it was observed that the %leaking were lowered when the DLCs were increased. If DLCs were rigorously the same, the obtained results in this release study would be even accentuated. These quite tricky results emphasize clearly the role of the surface chemistry over the drug release.
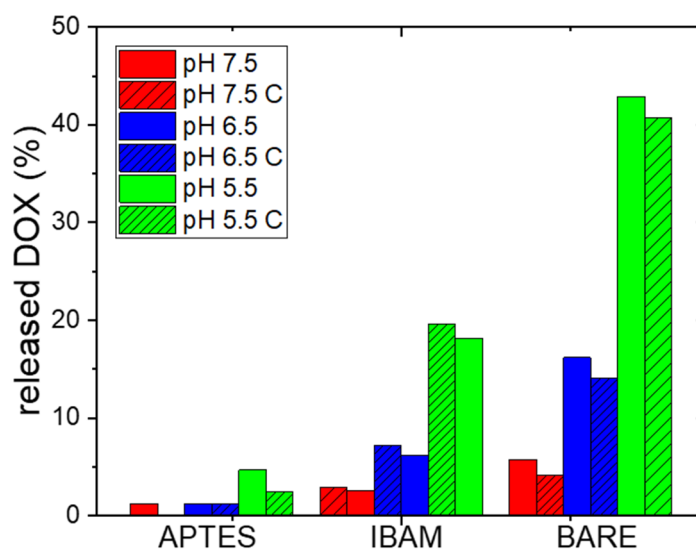
Figure 7. Representation of the total drug released over the 4 cycles (from Figure 6) as a function of the surface chemistry, the pH and the NIR light, being the latter applied or not (C).

Regarding these results but also those from the drug leaking study described above, it appears that APTES and IBAM retain more DOX as compared to BARE whatever the pH. Our data indicate that the APTES polysiloxane which bears the amines, but also IBAM, play a clear role in the DOX retention to the NPs as compared to the BARE surface. In our previous works, we reported that an APTES polysiloxane layer at the surface of CNTs@MS is able to load an important amount of drugs (≥100 % wt) acting as a kind of organic sponge attracting DOX at the CNT@MS@APTS surface but the DOX release was found low (below 5%). A combination of interactions was hypothesized through H-bonding and π-π stacking that are probably involved to ensure retention of DOX at this surface.[55] Thus at a fixed pH, the main parameter

determining the release of drugs between the three modified surfaces is probably the kind of interactions involved between the modified surface and the drugs. It is assumed that:

- For BARE NPs, the release is increased importantly by decreasing pH because the DOX-surface electrostatic interactions become lower than the solvation forces of the protonated DOX. DOX can thus diffuse freely out of the silica.

- For APTES, it appears that the DOX is better retained to the aminosilane surface, despite the electrostatic repulsion involved between the two molecules. This result is not really intuitive. It may be possible that APTES act as kinds of surface primers able to favor non electrostatic interactions such as H-bonds and π-stacking due to the underneath polysiloxane layer.

- For IBAM, the leaking effect is intermediate between these two situations.

Noteworthy, the amount of HSA adsorbed may also influence the drug release : a lower amount as for BARE (51.2 µg/mg) may facilitate the drug release while a higher amount as for APTES (81.6 µg/mg) may help to retain the drug.

CONCLUSION

In this work, we have addressed for the first time the use of IO@STMS NPs for their NIR light-induced photothermal effect combined with drug release. The main points of the article are the following:

i) By tracing temperature profiles upon NIR light and evaluating light-induced SAR, we showed that the NPs concentration and the laser power are key parameters of the photothermal properties. Photothermal SAR, which can reach values up to 2000 W.g^{-1} (at 1 W.cm^{-2}), appear as particularly competitive with the magnetothermal values already published

ii) Regarding the drug loading study of these core shell NPs with DOX, the pH of the drug impregnation aqueous solution was found to be the critical parameter determining the drug payload while the surface chemistry used: BARE, APTES or IBAM had a limited influence. Indeed, for instance, with IO@STMS@IBAM we have shown that a loading at pH = 7.5 allowed to reach DLCs up to 73%, a high DLC as compared to the literature, while at pH = 5.5, the DLC reached only 7%. Further, a coating of HSA wrapped around such core-shell NPs estimated at ca. 50-80 µg/mg IO@STMS (depending on the surface functionalization considered) was found to ensure limited drug leaking before the intended application.

iii) At last, to assess both the possibility of NIR photothermia combined with drug release from these IO@STMS@DOX@HSA core-shell systems, a cumulative release study was achieved upon 4 daily cycles in the presence or absence of NIR light. Even if the NIR light does not trigger the drug release, the combination of local photo-induced hyperthermia along with pH-induced drug delivery has been demonstrated, with a DOX final amount released depending strongly here on the surface chemistry used. This low pH-induced drug delivery (pH 5.5) may be beneficial for intracellular drug release in the lysosomal cell compartment.

In next works, a biological study with cancer cells is expected to evaluate the interactions of the NPs with the cells and the combined effect of photothermia and drug delivery for synergistic anti-tumor treatments.

Acknowledgements.

REFERENCES

[1] T. Lammers, S. Aime, W.E. Hennink, G. Storm, F. Kiessling, Theranostic nanomedicine, Accounts of Chemical Research. 44 (2011) 1029–1038.

[2] S.M. Janib, A.S. Moses, J.A. MacKay, Imaging and drug delivery using theranostic nanoparticles, Advanced Drug Delivery Reviews. 62 (2010) 1052–1063.

[3] K.Y. Choi, G. Liu, S. Lee, X. Chen, Theranostic nanoplatforms for simultaneous cancer imaging and therapy: current approaches and future perspectives, Nanoscale. 4 (2012) 330–342.

[4] S. Mura, P. Couvreur, Nanotheranostics for personalized medicine, Advanced Drug Delivery Reviews. 64 (2012) 1394–1416.

[5] T. Lammers, L.Y. Rizzo, G. Storm, F. Kiessling, Personalized Nanomedicine, Clin Cancer Res. 18 (2012) 4889–4894. https://doi.org/10.1158/1078-0432.CCR-12-1414.

[6] S. Laurent, D. Forge, M. Port, A. Roch, C. Robic, L. Vander Elst, R.N. Muller, Magnetic Iron Oxide Nanoparticles: Synthesis, Stabilization, Vectorization, Physicochemical Characterizations, and Biological Applications, Chem. Rev. 108 (2008) 2064–2110. https://doi.org/10.1021/cr068445e.

[7] M. Mahmoudi, S. Sant, B. Wang, S. Laurent, T. Sen, Superparamagnetic iron oxide nanoparticles (SPIONs): development, surface modification and applications in chemotherapy, Advanced Drug Delivery Reviews. 63 (2011) 24–46.

[8] D. Stanicki, L. Vander Elst, R.N. Muller, S. Laurent, D. Felder-Flesch, D. Mertz, A. Parat, S. Begin-Colin, G. Cotin, J.-M. Greneche, Iron-oxide Nanoparticle-based Contrast Agents, in: Contrast Agents for MRI, 2017: pp. 318–447.

[9] R. Hachani, M. Lowdell, M. Birchall, A. Hervault, D. Mertz, S. Begin-Colin, N.T.K. Thanh, Polyol synthesis, functionalisation, and biocompatibility studies of superparamagnetic iron oxide nanoparticles as potential MRI contrast agents, Nanoscale. 8 (2016) 3278–3287.

[10] H.B. Na, I.C. Song, T. Hyeon, Inorganic nanoparticles for MRI contrast agents, Advanced Materials. 21 (2009) 2133–2148.

[11] F. Mazuel, A. Espinosa, N. Luciani, M. Reffay, R. Le Borgne, L. Motte, K. Desboeufs, A. Michel, T. Pellegrino, Y. Lalatonne, C. Wilhelm, Massive Intracellular Biodegradation of Iron Oxide Nanoparticles Evidenced Magnetically at Single-Endosome and Tissue Levels, ACS Nano. 10 (2016) 7627–7638. https://doi.org/10.1021/acsnano.6b02876.

[12] L. Lartigue, D. Alloyeau, J. Kolosnjaj-Tabi, Y. Javed, P. Guardia, A. Riedinger, C. Péchoux, T. Pellegrino, C. Wilhelm, F. Gazeau, Biodegradation of Iron Oxide Nanocubes: High-Resolution In Situ Monitoring, ACS Nano. 7 (2013) 3939–3952. https://doi.org/10.1021/nn305719y.

[13] M. Tasso, M.A. Lago Huvelle, I. Diaz Bessone, A.S. Picco, Toxicity Assessment of Nanomaterials, in: S.K. Sharma, Y. Javed (Eds.), Magnetic Nanoheterostructures: Diagnostic, Imaging and Treatment, Springer International Publishing, Cham, 2020: pp. 383–446. https://doi.org/10.1007/978-3-030-39923-8_13.

[14] M. Tasso, F. Ghilini, M. Cathcarth, A.S. Picco, Toxicity Assessment of Nanoferrites, in: S.K. Sharma (Ed.), Spinel Nanoferrites: Synthesis, Properties and Applications, Springer International Publishing, Cham, 2021: pp. 233–314. https://doi.org/10.1007/978-3-030-79960-1_9.

[15] C. Blanco-Andujar, A. Walter, G. Cotin, C. Bordeianu, D. Mertz, D. Felder-Flesch, S. Begin-Colin, Design of iron oxide-based nanoparticles for MRI and magnetic hyperthermia, Nanomedicine. 11 (2016) 1889–1910.

[16] N. Lee, D. Yoo, D. Ling, M.H. Cho, T. Hyeon, J. Cheon, Iron oxide based nanoparticles for multimodal imaging and magnetoresponsive therapy, Chemical Reviews. 115 (2015) 10637–10689.

[17] E.A. Perigo, G. Hemery, O. Sandre, D. Ortega, E. Garaio, F. Plazaola, F.J. Teran, Fundamentals and advances in magnetic hyperthermia, Applied Physics Reviews. 2 (2015) 041302.

[18] P. Hugounenq, M. Levy, D. Alloyeau, L. Lartigue, E. Dubois, V. Cabuil, C. Ricolleau, S. Roux, C. Wilhelm, F. Gazeau, Iron oxide monocrystalline nanoflowers for highly efficient magnetic hyperthermia, The Journal of Physical Chemistry C. 116 (2012) 15702–15712.

[19] B. Thiesen, A. Jordan, Clinical applications of magnetic nanoparticles for hyperthermia, International Journal of Hyperthermia. 24 (2008) 467–474. https://doi.org/10.1080/02656730802104757.

[20] K. Maier-Hauff, F. Ulrich, D. Nestler, H. Niehoff, P. Wust, B. Thiesen, H. Orawa, V. Budach, A. Jordan, Efficacy and safety of intratumoral thermotherapy using magnetic iron-oxide nanoparticles combined with external beam radiotherapy on patients with recurrent glioblastoma multiforme, Journal of Neuro-Oncology. 103 (2011) 317–324.

[21] K. Maier-Hauff, R. Rothe, R. Scholz, U. Gneveckow, P. Wust, B. Thiesen, A. Feussner, A. von Deimling, N. Waldoefner, R. Felix, Intracranial thermotherapy using magnetic nanoparticles combined with external beam radiotherapy: results of a feasibility study on patients with glioblastoma multiforme, Journal of Neuro-Oncology. 81 (2007) 53–60.

[22] S. Stolik, J.A. Delgado, A. Pérez, L. Anasagasti, Measurement of the penetration depths of red and near infrared light in human "ex vivo" tissues, Journal of Photochemistry and Photobiology B: Biology. 57 (2000) 90–93. https://doi.org/10.1016/S1011-1344(00)00082-8.

[23] T.A. Henderson, L.D. Morries, Near-infrared photonic energy penetration: can infrared phototherapy effectively reach the human brain?, Neuropsychiatr Dis Treat. 11 (2015) 2191–2208. https://doi.org/10.2147/NDT.S78182.

[24] Y. Wang, K. Wang, J. Zhao, X. Liu, J. Bu, X. Yan, R. Huang, Multifunctional mesoporous silica-coated graphene nanosheet used for chemo-photothermal synergistic targeted therapy of glioma, Journal of the American Chemical Society. 135 (2013) 4799–4804.

[25] W.I. Choi, A. Sahu, Y.H. Kim, G. Tae, Photothermal cancer therapy and imaging based on gold nanorods, Annals of Biomedical Engineering. 40 (2012) 534–546.

[26] E.B. Dickerson, E.C. Dreaden, X. Huang, I.H. El-Sayed, H. Chu, S. Pushpanketh, J.F. McDonald, M.A. El-Sayed, Gold nanorod assisted near-infrared plasmonic photothermal therapy (PPTT) of squamous cell carcinoma in mice, Cancer Letters. 269 (2008) 57–66.

[27] J. Croissant, M. Maynadier, O. Mongin, V. Hugues, M. Blanchard-Desce, A. Chaix, X. Cattoën, M. Wong Chi Man, A. Gallud, M. Gary-Bobo, Enhanced two-photon fluorescence imaging and therapy of cancer cells via gold@ bridged silsesquioxane nanoparticles, Small. 11 (2015) 295–299.

[28] U. Chitgupi, Y. Qin, J.F. Lovell, Targeted Nanomaterials for Phototherapy, Nanotheranostics. 1 (2017) 38–58. https://doi.org/10.7150/ntno.17694.

[29] Nanospectra | Leveraging Nanoshells in the First True Focal Therapy, (n.d.). https://nanospectra.com/ (accessed November 19, 2021).

[30] J. Estelrich, M.A. Busquets, Iron Oxide Nanoparticles in Photothermal Therapy, Molecules. 23 (2018) 1567. https://doi.org/10.3390/molecules23071567.

[31] S. Shen, S. Wang, R. Zheng, X. Zhu, X. Jiang, D. Fu, W. Yang, Magnetic nanoparticle clusters for photothermal therapy with near-infrared irradiation, Biomaterials. 39 (2015) 67–74. https://doi.org/10.1016/j.biomaterials.2014.10.064.

[32] A. Espinosa, R. Di Corato, J. Kolosnjaj-Tabi, P. Flaud, T. Pellegrino, C. Wilhelm, Duality of Iron Oxide Nanoparticles in Cancer Therapy: Amplification of Heating Efficiency by Magnetic Hyperthermia and Photothermal Bimodal Treatment, ACS Nano. 10 (2016) 2436–2446. https://doi.org/10.1021/acsnano.5b07249.

[33] S. Cabana, A. Curcio, A. Michel, C. Wilhelm, A. Abou-Hassan, Iron Oxide Mediated Photothermal Therapy in the Second Biological Window: A Comparative Study between Magnetite/Maghemite Nanospheres and Nanoflowers, Nanomaterials. 10 (2020) 1548. https://doi.org/10.3390/nano10081548.

[34] P. Saint-Cricq, S. Deshayes, J.I. Zink, A.M. Kasko, Magnetic field activated drug delivery using thermodegradable azo-functionalised PEG-coated core–shell mesoporous silica nanoparticles, Nanoscale. 7 (2015) 13168–13172.

[35] S.-H. Hu, S.-Y. Chen, D.-M. Liu, C.-S. Hsiao, Core/Single-Crystal-Shell Nanospheres for Controlled Drug Release via a Magnetically Triggered Rupturing Mechanism, Advanced Materials. 20 (2008) 2690–2695.

[36] N. Griffete, J. Fresnais, A. Espinosa, C. Wilhelm, A. Bée, C. Ménager, Design of magnetic molecularly imprinted polymer nanoparticles for controlled release of doxorubicin under an alternative magnetic field in athermal conditions, Nanoscale. 7 (2015) 18891–18896.

[37] T.T.T. N'Guyen, H.T.T. Duong, J. Basuki, V. Montembault, S. Pascual, C. Guibert, J. Fresnais, C. Boyer, M.R. Whittaker, T.P. Davis, L. Fontaine, Functional Iron Oxide Magnetic Nanoparticles with Hyperthermia-Induced Drug Release Ability by Using a Combination of Orthogonal Click Reactions, Angewandte Chemie International Edition. 52 (2013) 14152–14156. https://doi.org/10.1002/anie.201306724.

[38] N.Ž. Knežević, I.I. Slowing, V.S.-Y. Lin, Tuning the release of anticancer drugs from magnetic iron oxide/mesoporous silica core/shell nanoparticles, ChemPlusChem. 77 (2012) 48–55.

[39] Q. Yue, J. Li, W. Luo, Y. Zhang, A.A. Elzatahry, X. Wang, C. Wang, W. Li, X. Cheng, A. Alghamdi, An interface coassembly in biliquid phase: Toward core–shell magnetic mesoporous silica microspheres with tunable pore size, J. Am. Chem. Soc. 137 (2015) 13282–13289.

[40] J. Kim, H.S. Kim, N. Lee, T. Kim, H. Kim, T. Yu, I.C. Song, W.K. Moon, T. Hyeon, Multifunctional uniform nanoparticles composed of a magnetite nanocrystal core and a mesoporous silica shell for magnetic resonance and fluorescence imaging and for drug delivery, Angewandte Chemie International Edition. 47 (2008) 8438–8441.

[41] A. Baeza, E. Guisasola, E. Ruiz-Hernández, M. Vallet-Regí, Magnetically triggered multidrug release by hybrid mesoporous silica nanoparticles, Chemistry of Materials. 24 (2012) 517–524.

[42] D. Mertz, O. Sandre, S. Bégin-Colin, Drug releasing nanoplatforms activated by alternating magnetic fields, Biochimica et Biophysica Acta (BBA) - General Subjects. 1861 (2017) 1617–1641. https://doi.org/10.1016/j.bbagen.2017.02.025.

[43] A. Hervault, N.T.K. Thanh, Magnetic nanoparticle-based therapeutic agents for thermo-chemotherapy treatment of cancer, Nanoscale. 6 (2014) 11553–11573.

[44] D. Mertz, S. Harlepp, J. Goetz, D. Bégin, G. Schlatter, S. Bégin-Colin, A. Hébraud, Nanocomposite Polymer Scaffolds Responding under External Stimuli for Drug Delivery and Tissue Engineering Applications, Advanced Therapeutics. 3 (2020) 1900143. https://doi.org/10.1002/adtp.201900143.

[45] E. Cazares-Cortes, S. Cabana-Montenegro, C. Boitard, E. Nehling, N. Griffete, J. Fresnais, C. Wilhelm, A. Abou-Hassan, C. Ménager, Recent insights in magnetic hyperthermia: From the "hot-spot" effect for local delivery to combined magneto-photo-thermia using magneto-plasmonic hybrids, Advanced Drug Delivery Reviews. (2018).

[46] R. Narayan, U.Y. Nayak, A.M. Raichur, S. Garg, Mesoporous Silica Nanoparticles: A Comprehensive Review on Synthesis and Recent Advances, Pharmaceutics. 10 (2018) 118. https://doi.org/10.3390/pharmaceutics10030118.

[47] Y. Wang, H. Gu, Core–Shell-Type Magnetic Mesoporous Silica Nanocomposites for Bioimaging and Therapeutic Agent Delivery, Advanced Materials. 27 (2015) 576–585.

[48] Z. Sun, X. Zhou, W. Luo, Q. Yue, Y. Zhang, X. Cheng, W. Li, B. Kong, Y. Deng, D. Zhao, Interfacial engineering of magnetic particles with porous shells: Towards magnetic core–Porous shell microparticles, Nano Today. 11 (2016) 464–482.

[49] J. Croissant, D. Salles, M. Maynadier, O. Mongin, V. Hugues, M. Blanchard-Desce, X. Cattoën, M. Wong Chi Man, A. Gallud, M. Garcia, Mixed periodic mesoporous organosilica nanoparticles and core–shell systems, application to in vitro two-photon imaging, therapy, and drug delivery, Chemistry of Materials. 26 (2014) 7214–7220.

[50] W. Zhao, H. Wang, H. Wang, Y. Han, Z. Zheng, X. Liu, B. Feng, H. Zhang, Light-responsive dual-functional biodegradable mesoporous silica nanoparticles with drug delivery and lubrication enhancement for the treatment of osteoarthritis, Nanoscale. 13 (2021) 6394–6399. https://doi.org/10.1039/D0NR08887K.

[51] S. Zhou, Q. Zhong, Y. Wang, P. Hu, W. Zhong, C.-B. Huang, Z.-Q. Yu, C.-D. Ding, H. Liu, J. Fu, Chemically engineered mesoporous silica nanoparticles-based intelligent delivery systems for theranostic applications in multiple cancerous/non-cancerous diseases, Coordination Chemistry Reviews. 452 (2022) 214309. https://doi.org/10.1016/j.ccr.2021.214309.

[52] Y. He, L. Shao, I. Usman, Y. Hu, A. Pan, S. Liang, H. Xu, A pH-responsive dissociable mesoporous silica-based nanoplatform enabling efficient dual-drug co-delivery and rapid clearance for cancer therapy, Biomater. Sci. 8 (2020) 3418–3429. https://doi.org/10.1039/D0BM00204F.

[53] F. Perton, M. Tasso, G.A. Muñoz Medina, M. Ménard, C. Blanco-Andujar, E. Portiansky, M.B.F. van Raap, D. Bégin, F. Meyer, S. Begin-Colin, D. Mertz, Fluorescent and magnetic stellate mesoporous silica for bimodal imaging and magnetic hyperthermia, Applied Materials Today. 16 (2019) 301–314. https://doi.org/10.1016/j.apmt.2019.06.006.

[54] M. Ménard, F. Meyer, C. Affolter-Zbaraszczuk, M. Rabineau, A. Adam, P.D. Ramirez, S. Bégin-Colin, D. Mertz, Design of hybrid protein-coated magnetic core-mesoporous silica shell nanocomposites for MRI and drug release assessed in a 3D tumor cell model, Nanotechnology. 30 (2019) 174001. https://doi.org/10.1088/1361-6528/aafe1c.

[55] C. Wells, O. Vollin-Bringel, V. Fiegel, S. Harlepp, B.V. der Schueren, S. Bégin-Colin, D. Bégin, D. Mertz, Engineering of Mesoporous Silica Coated Carbon-Based Materials Optimized for an Ultrahigh Doxorubicin Payload and a Drug Release Activated by pH, T, and NIR-light, Advanced Functional Materials. 28 (2018) 1706996. https://doi.org/10.1002/adfm.201706996.

[56] A. Adam, K. Parkhomenko, P. Duenas-Ramirez, C. Nadal, G. Cotin, P.-E. Zorn, P. Choquet, S. Bégin-Colin, D. Mertz, Orienting the Pore Morphology of Core-Shell Magnetic Mesoporous Silica with the Sol-Gel Temperature. Influence on MRI and Magnetic Hyperthermia Properties, Molecules. 26 (2021) 971. https://doi.org/10.3390/molecules26040971.

[57] Y. Wang, Y. Sun, J. Wang, Y. Yang, Y. Li, Y. Yuan, C. Liu, Charge-Reversal APTES-Modified Mesoporous Silica Nanoparticles with High Drug Loading and Release Controllability, ACS Applied Materials & Interfaces. 8 (2016) 17166–17175.

[58] Y. Mehmood, I.U. Khan, Y. Shahzad, R.U. Khan, S.H. Khalid, A.M. Yousaf, T. Hussain, S. Asghar, I. Khalid, M. Asif, S.U. Shah, Amino-decorated mesoporous silica nanoparticles for controlled sofosbuvir delivery, European Journal of Pharmaceutical Sciences. 143 (2020) 105184. https://doi.org/10.1016/j.ejps.2019.105184.

[59] F. Perton, S. Harlepp, G. Follain, K. Parkhomenko, J.G. Goetz, S. Bégin-Colin, D. Mertz, Wrapped stellate silica nanocomposites as biocompatible luminescent nanoplatforms assessed in vivo, Journal of Colloid and Interface Science. 542 (2019) 469–482. https://doi.org/10.1016/j.jcis.2019.01.098.

[60] D. Mertz, P. Tan, Y. Wang, T.K. Goh, A. Blencowe, F. Caruso, Bromoisobutyramide as an Intermolecular Surface Binder for the Preparation of Free-standing Biopolymer Assemblies, Advanced Materials. 23 (2011) 5668–5673. https://doi.org/10.1002/adma.201102890.

[61] A. Walter, C. Billotey, A. Garofalo, C. Ulhaq-Bouillet, C. Lefèvre, J. Taleb, S. Laurent, L. Vander Elst, R.N. Muller, L. Lartigue, Mastering the shape and composition of dendronized iron oxide nanoparticles to tailor magnetic resonance imaging and hyperthermia, Chemistry of Materials. 26 (2014) 5252–5264.

[62] W. Baaziz, B.P. Pichon, S. Fleutot, Y. Liu, C. Lefevre, J.-M. Greneche, M. Toumi, T. Mhiri, S. Begin-Colin, Magnetic iron oxide nanoparticles: reproducible tuning of the size and nanosized-dependent composition, defects, and spin canting, The Journal of Physical Chemistry C. 118 (2014) 3795–3810.

[63] G. Cotin, C. Blanco-Andujar, D.-V. Nguyen, C. Affolter, S. Boutry, A. Boos, P. Ronot, B. Uring-Lambert, P. Choquet, P.E. Zorn, D. Mertz, S. Laurent, R.N. Muller, F. Meyer, D.F. Flesch, S. Begin-Colin, Dendron based antifouling, MRI and magnetic hyperthermia properties of different shaped iron oxide nanoparticles, Nanotechnology. 30 (2019) 374002. https://doi.org/10.1088/1361-6528/ab2998.

[64] G. Cotin, C. Blanco-Andujar, F. Perton, L. Asín, J.M. de la Fuente, W. Reichardt, D. Schaffner, D.-V. Ngyen, D. Mertz, C. Kiefer, F. Meyer, S. Spassov, O. Ersen, M. Chatzidakis, G.A. Botton, C. Hénoumont, S. Laurent, J.-M. Greneche, F.J. Teran, D. Ortega, D. Felder-Flesch, S. Begin-Colin, Unveiling the role of surface, size, shape and defects of iron oxide nanoparticles for theranostic applications, Nanoscale. 13 (2021) 14552–14571. https://doi.org/10.1039/D1NR03335B.

[65] K. Zhang, L.-L. Xu, J.-G. Jiang, N. Calin, K.-F. Lam, S.-J. Zhang, H.-H. Wu, G.-D. Wu, B. Albela, L. Bonneviot, Facile large-scale synthesis of monodisperse mesoporous silica nanospheres with tunable pore structure, Journal of the American Chemical Society. 135 (2013) 2427–2430.

[66] J. Hai, H. Piraux, E. Mazarío, J. Volatron, N.T. Ha-Duong, P. Decorse, J.S. Lomas, P. Verbeke, S. Ammar, C. Wilhelm, J.-M.E.H. Chahine, M. Hémadi, Maghemite nanoparticles coated with human serum albumin: combining targeting by the iron-

acquisition pathway and potential in photothermal therapies, J. Mater. Chem. B. 5 (2017) 3154–3162. https://doi.org/10.1039/C7TB00503B.

[67] S. Cabana, A. Curcio, A. Michel, C. Wilhelm, A. Abou-Hassan, Iron Oxide Mediated Photothermal Therapy in the Second Biological Window: A Comparative Study between Magnetite/Maghemite Nanospheres and Nanoflowers, Nanomaterials. 10 (2020) 1548. https://doi.org/10.3390/nano10081548.

[68] C. Lozano-Pedraza, E. Plaza-Mayoral, A. Espinosa, B. Sot, A. Serrano, G. Salas, C. Blanco-Andujar, G. Cotin, D. Felder-Flesch, S. Begin-Colin, F. J. Teran, Assessing the parameters modulating optical losses of iron oxide nanoparticles under near infrared irradiation, Nanoscale Advances. 3 (2021) 6490–6502. https://doi.org/10.1039/D1NA00601K.

[69] S. Nemec, S. Kralj, C. Wilhelm, A. Abou-Hassan, M.-P. Rols, J. Kolosnjaj-Tabi, Comparison of Iron Oxide Nanoparticles in Photothermia and Magnetic Hyperthermia: Effects of Clustering and Silica Encapsulation on Nanoparticles' Heating Yield, Applied Sciences. 10 (2020) 7322. https://doi.org/10.3390/app10207322.

[70] J. Kolosnjaj-Tabi, S. Kralj, E. Griseti, S. Nemec, C. Wilhelm, A. Plan Sangnier, E. Bellard, I. Fourquaux, M. Golzio, M.-P. Rols, Magnetic Silica-Coated Iron Oxide Nanochains as Photothermal Agents, Disrupting the Extracellular Matrix, and Eradicating Cancer Cells, Cancers. 11 (2019) 2040. https://doi.org/10.3390/cancers11122040.

[71] P. Duenas-Ramirez, C. Bertagnolli, R. Müller, K. Sartori, A. Boos, M. Elhabiri, S. Bégin-Colin, D. Mertz, Highly chelating stellate mesoporous silica nanoparticles for specific iron removal from biological media, Journal of Colloid and Interface Science. 579 (2020) 140–151. https://doi.org/10.1016/j.jcis.2020.06.013.

[72] B. Li, S. Harlepp, V. Gensbittel, C.J.R. Wells, O. Bringel, J.G. Goetz, S. Begin-Colin, M. Tasso, D. Begin, D. Mertz, Near infra-red light responsive carbon nanotubes@mesoporous silica for photothermia and drug delivery to cancer cells, Materials Today Chemistry. 17 (2020) 100308. https://doi.org/10.1016/j.mtchem.2020.100308.

[73] J. Liu, C. Detrembleur, M.-C. De Pauw-Gillet, S. Mornet, L. Vander Elst, S. Laurent, C. Jérôme, E. Duguet, Heat-triggered drug release systems based on mesoporous silica nanoparticles filled with a maghemite core and phase-change molecules as gatekeepers, Journal of Materials Chemistry B. 2 (2014) 59–70.

[74] B. Chang, J. Guo, C. Liu, J. Qian, W. Yang, Surface functionalization of magnetic mesoporous silica nanoparticles for controlled drug release, Journal of Materials Chemistry. 20 (2010) 9941–9947.

[75] 栄治早川, 邦敏古家, 英雄上野, 徳幸黒田, 圭雄森山, 明近藤, Visible Absorption and Proton Nuclear Magnetic Resonance Studies on the Self-Association of Doxorubicin in Aqueous Solution, Chemical & Pharmaceutical Bulletin. 39 (1991) 1009–1012. https://doi.org/10.1248/cpb.39.1009.

[76] M. Menozzi, L. Valentini, E. Vannini, F. Arcamone, Self-association of doxorubicin and related compounds in aqueous solution, Journal of Pharmaceutical Sciences. 73 (1984) 766–770. https://doi.org/10.1002/jps.2600730615.

[77] E. Tasca, J. Alba, L. Galantini, M. D'Abramo, A.M. Giuliani, A. Amadei, G. Palazzo, M. Giustini, The self-association equilibria of doxorubicin at high concentration and ionic strength characterized by fluorescence spectroscopy and molecular dynamics simulations, Colloids and Surfaces A: Physicochemical and Engineering Aspects. 577 (2019) 517–522. https://doi.org/10.1016/j.colsurfa.2019.06.005.

[78] E. Tasca, M. D'Abramo, L. Galantini, A.M. Giuliani, N.V. Pavel, G. Palazzo, M. Giustini, A Stereochemically Driven Supramolecular Polymerisation, Chemistry – A European Journal. 24 (2018) 8195–8204. https://doi.org/10.1002/chem.201800644.